Single atom cobalt catalyst derived from co-pyrolysis of vitamin B_{12} and graphitic carbon nitride for PMS activation to degrade emerging pollutants

Shizong Wang [a,b], Jianlong Wang [a,b,*]

[a] Laboratory of Environmental Technology, INET, Tsinghua University, Beijing 100084, PR China
[b] Beijing Key Laboratory of Radioactive Wastes Treatment, Tsinghua University, Beijing 100084, PR China

ARTICLE INFO

ABSTRACT

This study prepared the carbon-supported cobalt catalyst (Co-C-X) for activating peroxymonosulfate (PMS), and investigated the effect of co-pyrolysis temperature of graphitic carbon nitride (g-C_3N_4) and vitamin B_{12} on the catalytic activity. It was found that with the increase of co-pyrolysis temperature, the catalytic activity of Co-C-X increased, due to the different coordination structures of cobalt. At 500 °C (Co-C-500), cobalt existed as CoO; while it was single atom Co at 600 °C (Co-C-600); and small size CoO at 700 °C (Co-C-700). Co-C-X could activate PMS to produce hydroxyl radicals, sulfate radicals, high-valent cobalt-oxo and singlet oxygen, which depended on the pyrolysis temperature. Although Co-C-700 had the highest catalytic activity, the leaching cobalt was also highest (3.23 mg/L), compared with that of Co-C-500 (0.27 mg/L) and Co-C-600 (0.14 mg/L). Co-C-600 had fast degradation for atrazine, nitrobenzene, bisphenol A, phenol and 4-chlorophenol, which also had wide pH range and high tolerance to inorganic ions.

1. Introduction

Carbon-supported metal single-atom catalysts (M-C-SACs) have received wide attention in the field of catalysis due to its high utilization of metal atom and superior catalytic performance [1–3]. Central metal atoms are widely recognized as the active sites of M-C-SACs [4–6]. Difference of central metal atoms largely determined the catalytic properties of M-C-SACs. To now, transition metal atoms (e.g. Fe and Co) and noble metal atoms (e.g. Pt and Au) are usually used as the central metal atoms for M-C-SACs [2]. Due to their own Fenton-like catalytic activity, transition metal atoms (e.g. Fe and Co) have been widely adopted as central metal atoms for the synthesis of Fenton-like catalysts [7,8] that are employed to activate chemical oxidants such as H_2O_2 and persulfate for the removal of recalcitrant organic pollutants [9].

Central metal atoms may dissolve in the process of Fenton-like process [10]. It is thus necessary to increase its stability of central metal atoms. Nitrogen atom on the carbon substrate can strongly bind with iron and cobalt atoms, which promoted the kinetic stability and thermodynamic stability of iron and cobalt [11–13]. Therefore, nitrogen-doped carbon materials have been broadly adopted to prepare M-C-SACs. Li et al. firstly synthesized Co-C-SACs in which CoN_4 was considered as the active sites that presented superior catalytic activity to

peroxymonosulfate (PMS) [14]. Gao et al. synthesized Co-C-SACs in which CoN_4 active sites exhibited much higher reaction kinetic constant and mass activity than Co nanocrystals [15].

In addition to the types of central metal atoms, the coordination structures of central metal atoms mainly regulate the catalytic activity of M-C-SACs [16–18]. Different coordination environments of cobalt induced different activation mechanisms of PMS [19,20]. Correspondingly, different reactive species including singlet oxygen, radicals and surface-mediated electron transfer were identified in the system of M-C-SACs/PMS. How to adjust the activation mechanism for PMS by changing the coordination structures of central metal sites is highly desired for the development of adjustable oxidation process based on the wastewater components.

The objective of this study was to regulate the activation mechanism for PMS by changing the coordination structures of Co towards the degradation of emerging organic pollutants in aqueous solution. In this study, co-pyrolysis of graphitic carbon nitride (g-C_3N_4) and vitamin B12 was adopted to prepare carbon-supported Co single-atom catalyst, while the coordination structure of Co was modulated by changing the co-pyrolysis temperature.

---

2. Materials and methods

2.1. Chemicals

Sulfamethoxazole (SMX, 98% purity), PMS (KHSO$_5$·0.5KHSO$_4$·0.5 K$_2$SO$_4$), urea (≥99.5% purity), 2,2′-azinobis(3-ethylbenzothiazoline −6-sulfonic acid ammonium salt (ABTS), vitamin B12 (98% purity), sodium nitrate (≥99% purity), 5,5-Dimethyl-1-pyrroline N-oxide (DMPO, 97% purity), methyl phenyl sulfoxide (PMSO, >98% purity), methyl phenyl sulfone (PMSO$_2$, >97% purity) and 4-amino-2,2,6,6-tetramethylpiperidine (TEMP, >98% purity) were purchased from Shanghai Aladdin Biochemical Technology Co., Ltd. Shanghai Macklin Biochemical Co., Ltd provided the following chemicals: sodium chloride (99.5% purity), sodium carbonate (≥99.5% purity), sodium sulfate (99% purity), tert-butanol (≥99% purity), sodium hydroxide (97% purity), ethanol (99.7% purity) and p-benzoquinone (97% purity). Sulfuric acid was supplied by Beijing Tong Guang Fine Chemicals Company.

2.2. Synthesis of Co-C-X

Graphitic carbon nitride (g-C$_3$N$_4$) was synthesized by thermal condensation of urea at 550 °C for 2 h with a heating rate of 10 °C/min.

Co-C-X was prepared by the pyrolysis of the mixture of vitamin B$_{12}$ and g-C$_3$N$_4$. Specially, 0.1 g vitamin B$_{12}$ was dissolved into the deionized water and stirred for 10 min. Thereafter, 0.4 g g-C$_3$N$_4$ was added into the vitamin B$_{12}$ solution and stirred for 3 h. The mixed solution was freeze-drying. The obtained solid was placed into the tube furnace. The tube furnace was heated to desired temperature at a heating rate of 10 °C/min and remained for 2 h under the atmosphere of nitrogen gas. The tube furnace was naturally cooled. The obtained solid was denoted as Co-C-X in which X represented the pyrolysis temperature.

2.3. Catalytic activity and stability of Co-C-X

The catalytic activity of Co-C-X was characterized by the SMX removal efficiency and mineralization efficiency. In brief, quantified SMX stock solution and Co-C-X were sequentially added into the 100-mL bottle in which there was 60-mL solution in total. Experiments were initiated by adding PMS stock solution. Samples were taken at regular time, and filtered through 0.45 μm Teflon membrane and immediately quenched by saturated thiosulfate solution (20 μL). To investigate the effect of different parameters on the SMX degradation, the experimental parameters were adjusted accordingly. Sodium hydroxide (1 M) and sulfuric acid (1 M) were used to adjust the solution pH. All the experiments were conducted in duplicate.

2.4. Characterization and analytic methods

Co-C-X was characterized by transmission electron microscope (TEM), high angle circular dark field scanning transmission electron microscope (HADDF-STEM), X-ray diffraction (XRD), X-ray photoelectron spectroscopy (XPS), Raman and X-ray absorption fine structure (XAFS). The content of iron in the Co-C-X was determined using inductively coupled plasma mass spectrometry (ICP-MS).

The concentration of targeted organic pollutants including SMX, atrazine, nitrophenol, bisphenol, 4-chlorophenol and phenol was determined by HPLC. The detailed conditions have been described in our previous studies [21]. Mineralization efficiency of targeted organic pollutants was measured by a TOC analyzer.

To identify the reactive species in the system of Co-C-X/PMS, the scavengers of reactive species were added into the solution. The used scavengers in this study were as follows: tertiary butanol as scavenger of hydroxyl radicals; ethanol as scavenger of hydroxyl radicals and sulfate radicals, respectively; benzoquinone as scavenger of superoxide radicals [22,23]. In addition to quenching experiments, electron spin resonance (ESR) was employed using DMPO and TEMP as trapping agents.
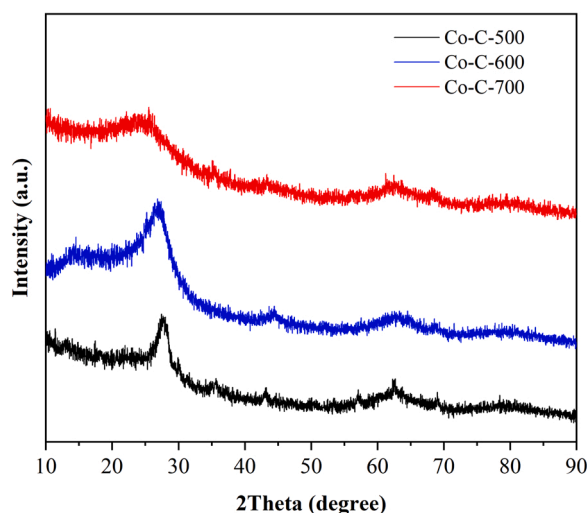

**Fig. 1.** XRD images of Co-C-500, Co-C-600 and Co-C-700.

The high-valent cobalt-oxo was determined by detecting the PMSO$_2$ during the process of PMSO degradation experiments [24]. The PMS concentration was determined with 2,2′-azino-bis(3-ethyl-benzothiazoline-6-sulfonic acid) (ABTS) method using a UV/Vis spectrophotometer (PerkinElmer Lambda 950) at 735 nm.

3. Results and discussion

3.1. Characterization of Co-C-X

Fig. 1 shows the XRD figures of Co-C-X. Pyrolysis temperature changed the structure of Co-C-X. When the pyrolysis temperature was 500 °C, the diffraction peak of g-C$_3$N$_4$ appeared at 27.8°, which is attributed to (0 0 2) facet of g-C$_3$N$_4$ (JCPDS 87–1526). In addition, the diffraction peaks were found at 43.3° and 62.7°, suggesting the presence of CoO (JCPDS 02–1217). When the pyrolysis temperature was increased to 600 °C, the diffraction peaks of g-C$_3$N$_4$ and CoO disappeared. Instead, the diffraction peak of graphitic carbon at 26.6° and 44.2° were observed, corresponding to (0 0 2) and (1 0 0) facets of graphitic carbon (JCPDS 25–0284). When the pyrolysis temperature was increased to 700 °C, the diffraction peaks of graphitic carbon became broader compared to that obtained at the pyrolysis temperature of 600 °C, which could be due to high content of nitrogen and cobalt into the carbon framework [25]. In addition, the characteristic peak of CoO occurred, which could be due to the fission of Co-N bond at 700 °C resulting in the aggregation of cobalt and combination of cobalt and oxygen [26]. For Co-C-X obtained at 600 °C, no diffraction peaks of cobalt and cobalt oxides indicates that cobalt on the Co-C-600 was amorphous and highly dispersed. The structure of g-C$_3$N$_4$ changed with the pyrolysis temperature in which g-C$_3$N$_4$ became unstable when the pyrolysis temperature reached 600 °C [27], which resulted in the decomposition of g-C$_3$N$_4$ and the formation of graphitic carbon.

XPS spectrums further confirmed the presence of carbon, nitrogen, oxygen and cobalt (Table S1). The atomic percentage of nitrogen decreased with the increase of calcination temperature. In contrast, the atomic percentages of carbon, oxygen and cobalt increased with the increase of temperature. The change of elemental atomic percentage might be due to the interaction between g-C$_3$N$_4$ and vitamin B12 under different pyrolysis temperatures. With the increase of pyrolysis temperature, more nitrogen atoms would be removed via forming ammonia gas [28] resulting in the decrease of nitrogen atomic percentage. In contrast, the atomic percentages of other elements increased. Fig. S1 presented the high resolution of C1s. For Co-C-500, the components of C1s included C-C/C=C (284.7 eV), C-O (286 eV), C=N (287.8 eV,
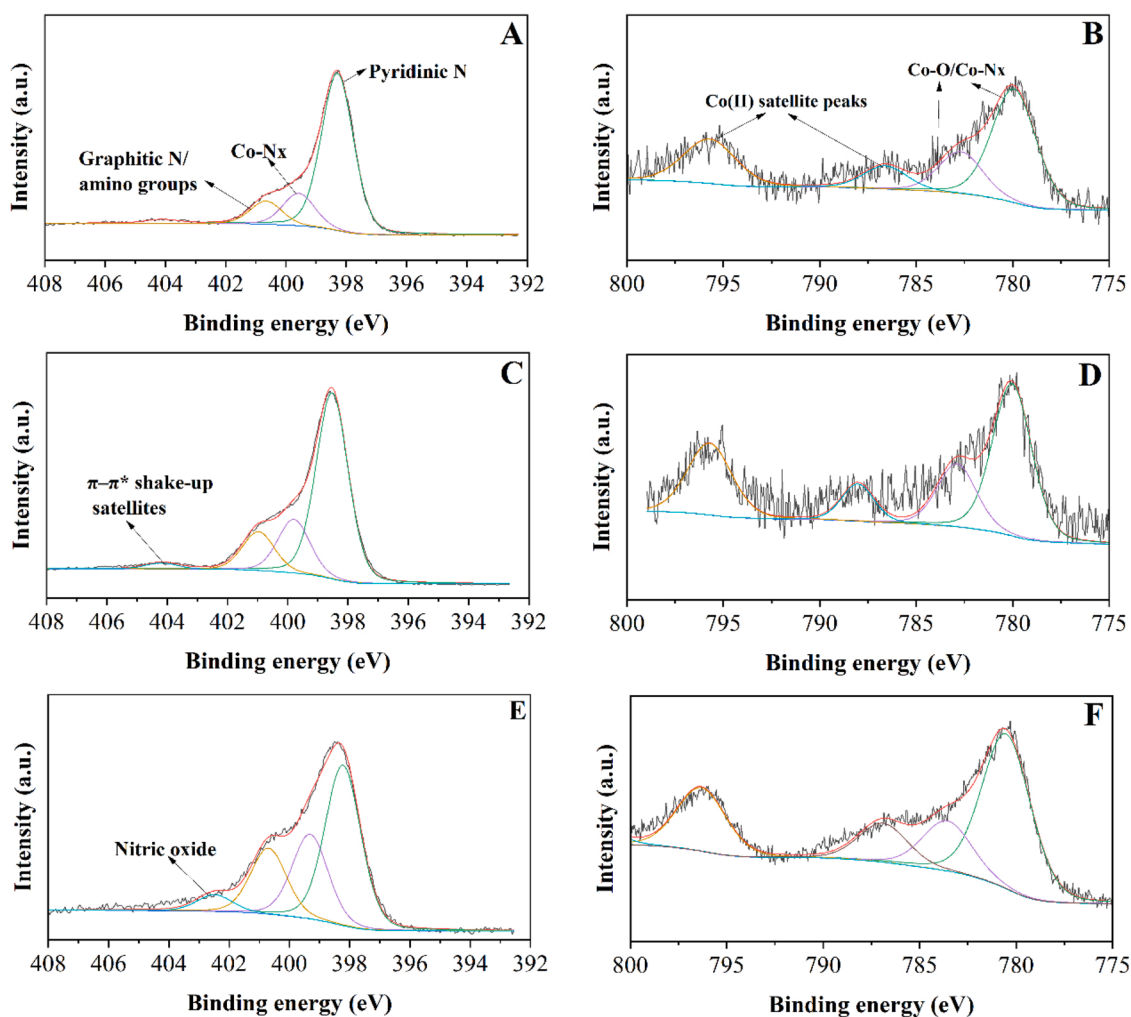
Fig. 2. High resolution of N1s and Co2p for Co-C-X. (A) N1s of Co-C-500 (B) Co2p of Co-C-500 (C) N1s of Co-C-600 (D) Co2p of Co-C-600 (E) N1s of Co-C-700 (F) Co2p of Co-C-700.

sp^2-hybridized carbon bonded to N atom inside the triazine rings) and C-N (288.7 eV, sp^2-hybridized carbon in the triazine ring bonded to the amino group) [29,30]. For Co-C-600, the components of C1s included C-C/C=C (284.7 eV), C-O (286 eV), C=N (287.8 eV, sp^2-hybridized carbon bonded to N atom inside the triazine rings) and π-excitation (293.7 eV) [31]. For Co-C-700, the components of C1s contained C-C/C=C (284.7 eV), C-O (286 eV), C-N (287.3 eV) and C=O (288.9 eV) [32]. The different components of C1s suggested the different structures of Co-C-X, which is consistent with the XRD results.

For the high resolution of O1s (Fig. S2), Co-C-X was consisted of three components: Co-O/C=O (~530.7 eV), -OH (~532.1 eV) and adsorbed H_2O (~533.6 eV) [33,34].

For the high resolution of N1s (Fig. 2A, C and E), Co-C-X could be divided into three components: pyridinic N, Co-Nx and graphitic N, respectively [35,36]. For the high resolution of Co2p (Fig. 2B, D and F), it can be divided into four components in which the peaks located at around 780.0 and 782.6 eV corresponded to Co-O/Co-Nx [37,38], while the other two peaks were the satellite peaks [39,40]. The binding energy of each component of N1s and Co2p changed with the pyrolysis temperature, further proving that pyrolysis temperature caused the variation of Co-C-X structures. The results of ICP-MS showed the cobalt content was 1.03 wt%, 1.40 wt% and 4.35%, respectively for Co-C-500, Co-C-600 and Co-C-700.

Raman spectrum of Co-C-X was also investigated. Two significant peaks located at around 1350 and 1570 cm^{-1}, respectively, were found (Fig. S3), which corresponded to the defect of carbon atom crystal (I_D) and graphitic phase (I_G) [41]. The ratio of I_D to I_G usually represents the defective intensity of carbonaceous materials [42]. In this study, this ratio was 1.08, 1.16 and 1.11, respectively for Co-C-500, Co-C-600 and Co-C-700, suggesting that Co-C-600 possessed more defective sites than Co-C-500 and Co-C-700. Defective sites could anchor metal atom that contributed to the formation of metal single atom active sites [43].

Surface area of Co-C-X was determined using N_2 adsorption curve. The adsorption curve for Co-C-X followed the type III isotherm (Fig. S4A). The surface area was calculated as 34.8, 43.5 and 60.1 m^2/g, respectively for Co-C-500, Co-C-600 and Co-C-700. The hysteresis loop belonged to H3 hysteresis loop, indicating that Co-C-X was mainly consisted of mesoporous [44]. Pore distribution was shown in Fig. S4B. The peaks appeared at 30.3, 46.1 and 49.6 nm, respectively for Co-C-500, Co-C-600 and Co-C-700, further confirming that Co-C-X was mainly consisted of mesoporous. Moreover, the average pore diameter also increased with the pyrolysis temperature, reaching 33.9, 34.6 and 50.6 nm. The large pore size would contribute to mass transportation [45].

TEM was used to observe the morphology of Co-C-X as shown in Fig. 3. The stacked layer structures were found for Co-C-X. There was significant lattice fringe with lattice spacing of 0.21 nm for Co-C-500 and Co-C-700 (Fig. 3A and Fig. 3C), which corresponded to (2 0 0) facet of CoO [46], while there was no lattice fringe for Co-C-600 (Fig. 3B), suggesting that no cobalt oxide formed. HADDF-STEM was used to observe the morphology of Co-C-600. Bright dot was observed (red circle), demonstrating that cobalt existed as single atom for
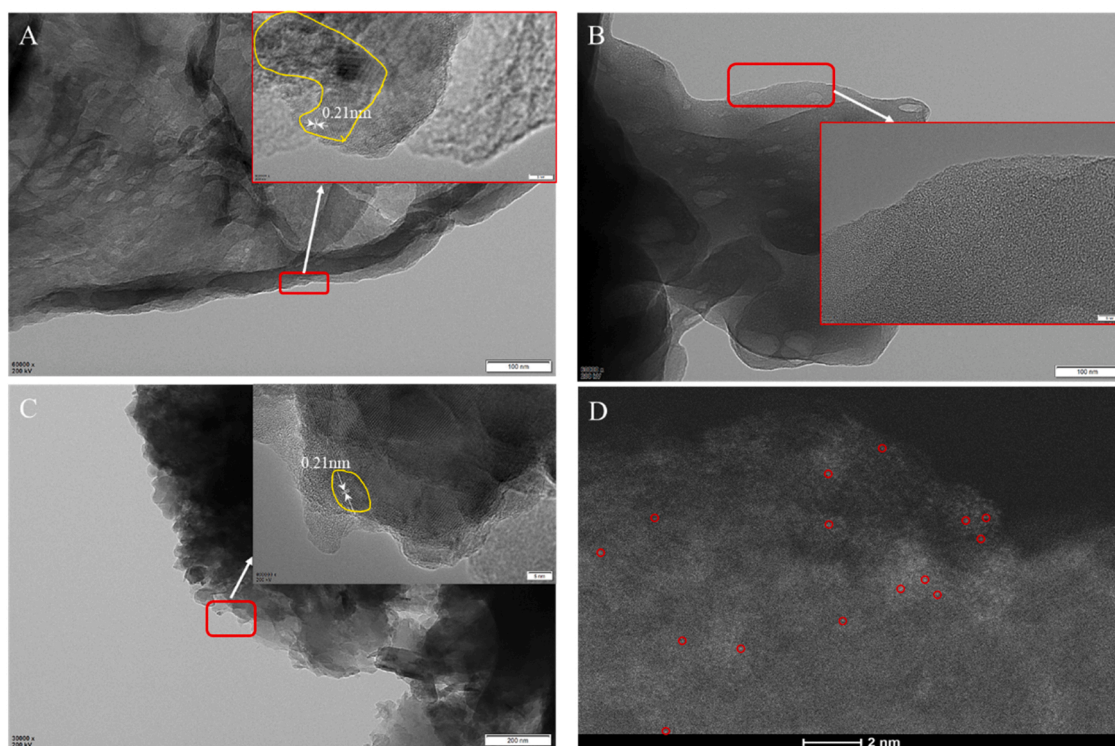
Fig. 3. Morphologies of Co-C-X (A) TEM image of Co-C-500; (B) TEM image of Co-C-600; (C) TEM image of Co-C-700; (D) HADDF-STEM image of Co-C-600.
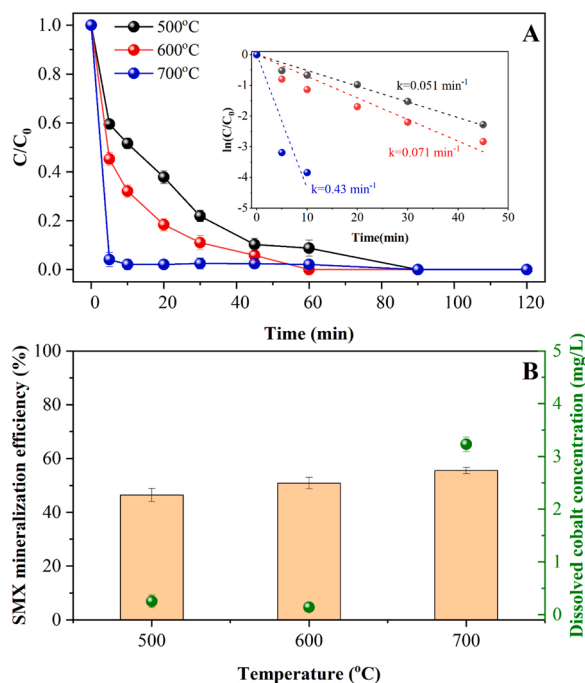

Fig. 4. Catalytic activity of Co-C-X for PMS (A) SMX degradation (B) SMX mineralization. [SMX]= 0.04 mM, [PMS]= 0.4 mM, Co-C-X dosage of 0.1 g/L, pH 3.2, 25 °C.

Table 1
Comparison of PMS utilization efficiency among different catalysts.

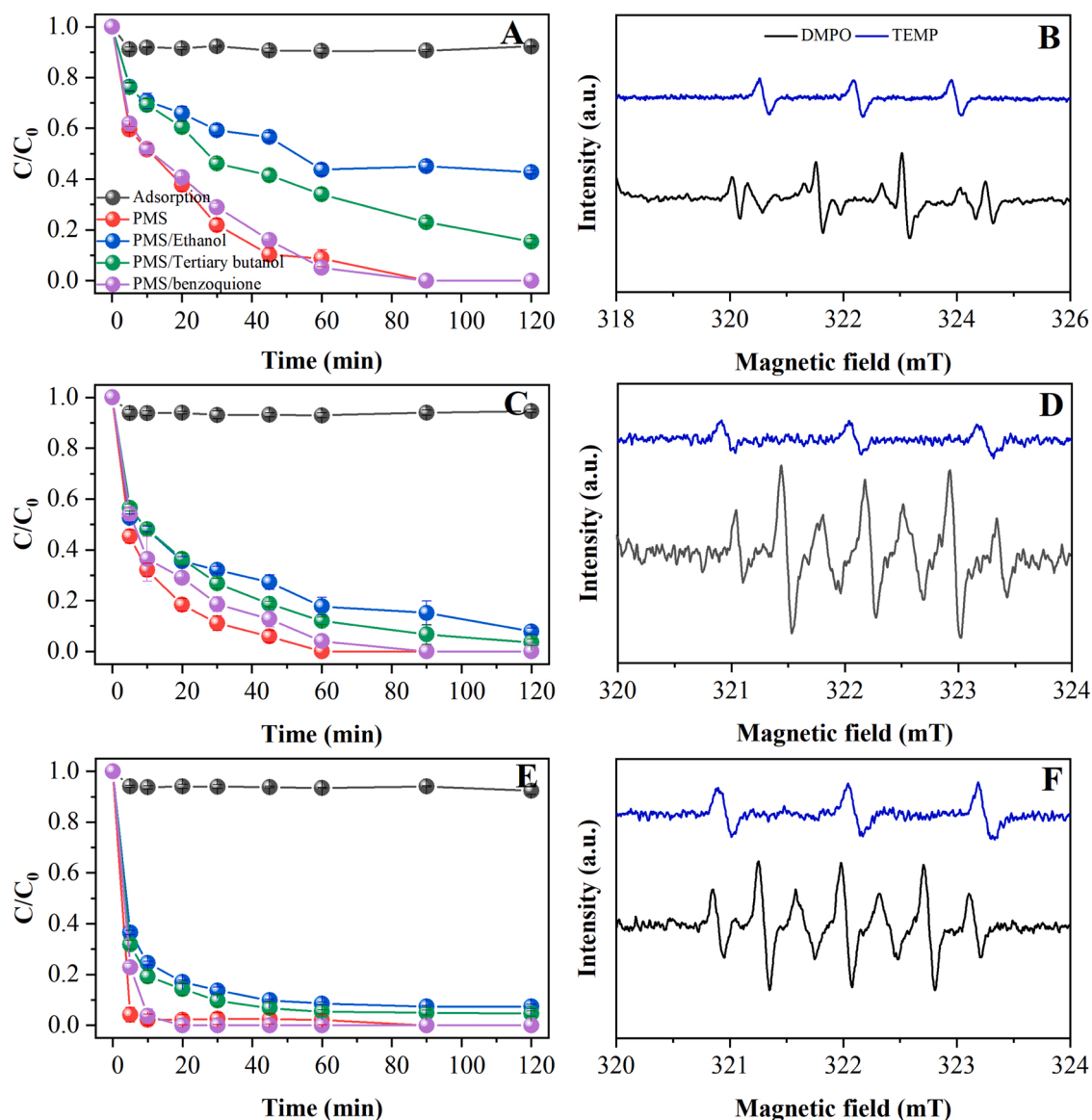| Catalysts	ΔTOC (mg/L)	ΔPMS (mM)	Dosage (g/L)	PUE (mg TOC/ (mMPMS* g catalyst)	References
Fe-N-O-GC-350	1.55	0.36	0.1	43.1	[47]
Cu-LaMnO$_3$	0.52	0.82	0.2	3.2	[48]
Fe-Co-O-g-C$_3$N$_4$	1.05	0.72	0.2	7.3	[49]
NiCo$_2$O$_4$-EG	0.77	0.3	0.06	42.7	[50]
SA-Cu/rGO	4.69	1.3	0.1	36.1	[51]
Fe-N$_4$-PC-2	3.45	0.3	0.03	383.3	[52]
Co-C-500	2.20	0.4	0.1	55.0	
Co-C-600	2.41	0.4	0.1	60.3	This study
Co-C-700	2.63	0.4	0.1	65.8	

3.2. Catalytic activity of Co-C-X

The catalytic activity of Co-C-X for PMS was investigated by conducting the degradation of sulfamethoxazole (SMX). Significant SMX degradation was observed in the presence of Co-C-X. The SMX degradation followed pseudo first-order kinetics. With the increase of pyrolysis temperature, the pseudo first-order kinetics constant (k) increased achieving 0.051, 0.071 and 0.43 min^{-1}, respectively for Co-C-500, Co-C-600 and Co-C-700 (Fig. 4A). Similarly, the mineralization efficiency of SMX increased with the pyrolysis temperature reaching 46.4%, 50.8% and 55.5%, respectively for Co-C-500, Co-C-600 and Co-C-700 (Fig. 4B).

In addition, no PMS was finally detected in solution, further demonstrating that PMS was completely activated. PMS utilization efficiency (PUE) was evaluated based on the following equation and compared to that reported in the previous studies.

$$PUE = \Delta TOC/(\Delta PMS * catalyst\ dosage) \qquad (1)$$

Where ΔTOC means the mineralization efficiency of SMX (mg);

Co-C-600. For Co-C-500 and Co-700, the size of CoO was different (yellow line area). The size of CoO became smaller at 700 °C than at 500 °C, which might be due to difference of cobalt dispersion degree as shown in Fig. 3C and the content of carbon and nitrogen on the Co-C-X.

Fig. 5. Identification of reactive species occurred in the systems of Co-C-X/PMS (A) quenching experiments for Co-C-500 (B) ESR spectrum for for C-C-500 (C) quenching experiments for Co-C-600 (D) ESR spectrum for Co-C-600 (E) quenching experiments for Co-C-700 (F) ESR spectrum for Co-C-700. [SMX]= 0.04 mM, [PMS]= 0.4 mM, [Ethanol]= [Tertiary butanol]= 200 mM, [Benzoquione]= 10 mM, pH 3.2, 25 °C.

ΔPMS represented the consumed amount of PMS in the reaction process (mg).

PMS utilization efficiency among different catalysts was summarized [47–52] and compared (Table 1).

Cobalt leaching is directly related to the catalytic stability of Co-C-X. Therefore, the concentration of cobalt ions in solution was measured eventually. The concentration of dissolved cobalt reached the maximum (3.23 mg/L) for Co-C-700, while for Co-C-500 and Co-C-600, the concentration of dissolved cobalt was 0.27 and 0.14 mg/L, respectively, indicating that cobalt in the structure of Co-C-600 had the best stability that could be due to the formation of Co-N bond of single atom cobalt [53]. The high dissolved concentration of cobalt for Co-C-700 could be due to the decrease of nitrogen content at 700 °C that decreased the stability of cobalt [54].

3.3. SMX degradation mechanism in the system of Co-C-X/PMS

For Co-C-500, Co-C-600 and Co-C-700, the adsorption made minor contribution to SMX degradation (less than 10%) (Fig. 5), indicating that SMX degradation was mainly due to the reactive species derived from PMS. The reactive species were thus identified in the system of Co-C-X/PMS using both quenching experiments and ESR techniques. For Co-C-500, the addition of ethanol (the scavenger as both hydroxyl radicals and sulfate radicals) and tertiary butanol (the scavenger as hydroxyl radicals) exhibited obvious inhibition on the SMX degradation (Fig. 5A). The final SMX removal efficiency achieved 57.4% and 84.7% after addition of ethanol and tertiary butanol, respectively. Benzoquinone that is usually used as scavenger of superoxide radicals had no significant effect on SMX degradation. It is thus concluded that both hydroxyl radicals and sulfate radicals contributed to the SMX degradation in which sulfate radicals dominated.

ESR spectrum further confirmed the occurrence of hydroxyl radicals and sulfate radicals (Fig. 5B). In addition to radicals, singlet oxygen was also found, suggesting that partial PMS was activated to produce singlet oxygen. It is well known that water could react with singlet oxygen at a rate constant of $\sim 10^5$ M^{-1}s^{-1}. In most cases, water is media and its concentration is much higher than organic pollutants. It is assumed that singlet oxygen makes major contribution to the degradation of organic

compounds. The reaction rate of singlet oxygen with organic pollutants is required to be higher than 10^8 $M^{-1}s^{-1}$ from the view point of competitive kinetics. Considering the low reaction rate of singlet oxygen with SMX ($\sim10^4$ $M^{-1}s^{-1}$) [55,56], it is thus concluded that the contribution of singlet oxygen to the SMX degradation was minor.

For Co-C-600, the addition of ethanol, tertiary butanol and benzoquinone exhibited slightly inhibition on the SMX degradation (Fig. 5C), indicating that sulfate radicals, hydroxyl radicals and superoxide radicals made minor contribution to SMX degradation in which hydroxyl radicals and sulfate radicals made higher contribution than superoxide radicals. No signal of hydroxyl radicals and sulfate radicals was found after the addition of DMPO in the spectrum of ESR (Fig. 5D). Instead, a characteristic of DMPOX was found, which could be the direct oxidation of DMPO or sequential oxidation of DMPO involving sulfate radicals [57]. After addition of TEMP, a signal of singlet oxygen was found, indicating the occurrence of singlet oxygen.

For Co-C-700, the addition of tertiary butanol and ethanol decreased the SMX degradation rate. But the removal efficiency of SMX finally achieved 92.7% and 95.4%, respectively (Fig. 5E). Similar to Co-C-500 and 600, benzoquinone had no significant effect on the SMX degradation, suggesting that superoxide radicals made minor contribution to SMX degradation. ESR spectrums showed the DMPOX signal after addition of DMPO and singlet oxygen after addition of TEMP (Fig. 5F).

In addition to radicals and singlet oxygen, high-valent cobalt-oxo could contribute to the SMX degradation. To verify the contribution of high-valent cobalt-oxo, PMSO degradation experiments were conducted to investigate whether there was $PMSO_2$ that was considered as the transformation products of PMSO by high-valent metal via electron transfer [24]. In all the experiments, PMSO was completely removed (Fig. S5). $PMSO_2$ was found in all the experiments, but its concentration increased with the pyrolysis temperature of Co-C-X. The maximum concentration of $PMSO_2$ was 0.022, 0.047 and 0.049 mM, respectively for Co-C-500, Co-C-600 and Co-C-700. This suggested that the concentration of high-valent cobalt-oxo increased with the pyrolysis temperature. The maximum concentration of $PMSO_2$ accounted for of 5.5%, 11.5% and 12.3% of the initially applied PMSO, respectively, it is thus concluded that high-valent cobalt made minor contribution to SMX degradation.

The steady-state concentration of hydroxyl radicals and sulfate radicals were roughly estimated using nitrobenzene and atrazine as probe compounds. Nitrobenzene has high reaction rate with hydroxyl radicals (3.9×10^9 $M^{-1}s^{-1}$), but low reaction rate with sulfate radicals ($<10^6$ $M^{-1}s^{-1}$) [22]. Thus, it can be used to determine the steady-state concentration of hydroxyl radicals. For atrazine, it has almost the same reaction rate of sulfate radicals and hydroxyl radicals (2.6×10^9 $M^{-1}s^{-1}$) [58,59]. It can be thus used to determine the total steady-state concentration of sulfate radicals and hydroxyl radicals. The degradation of nitrobenzene and atrazine was depicted in Fig. S6. Significant degradation of nitrobenzene and atrazine was found. Their degradation followed the pseudo first-order kinetics, and thus the pseudo first-order kinetic constant was determined. The calculated concentration of hydroxyl radicals and sulfate radicals was listed in Table S2. The steady-state concentration of radicals increased with the pyrolysis temperature of Co-C-X, achieving 2.15×10^{-13}, 2.33×10^{-13} and 2.65×10^{-13} M for Co-C-500, Co-C-600 and for Co-C-700, respectively. In addition, for Co-C-500 and Co-C-600, the steady-state concentration of hydroxyl radicals was higher than that of sulfate radicals, while the steady-state concentration of hydroxyl radicals was lower than that of sulfate radicals for Co-C-700, indicating that different activation mechanisms of Co-C-X were involved in PMS activation.

The direct electron transfer between PMS and SMX mediated by carbonaceous materials could result in the SMX degradation [60]. Thus, cyclic voltammetry was used to verify the contribution of direct electron transfer. Compared to the glassy carbon electrode, the Co-C-X-coated glassy carbon electrode showed higher current (Fig. S7), suggesting that Co-C-X could act as electron mediator. The maximum current was in
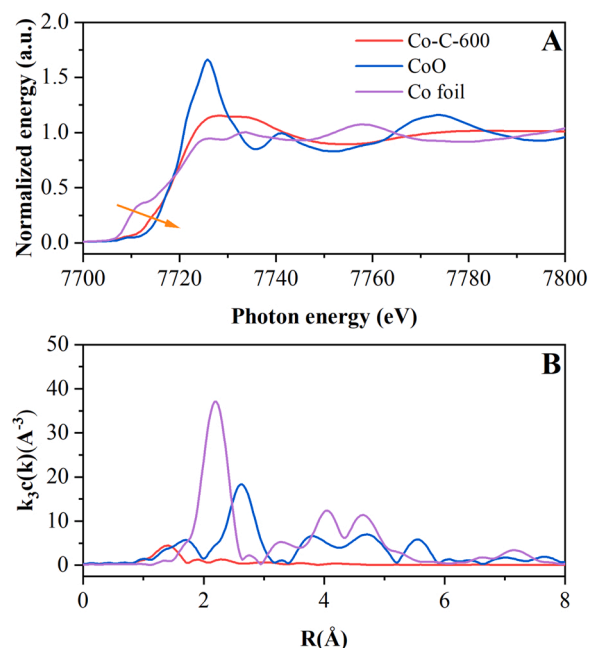

Fig. 6. Analysis of cobalt coordination structure for Co-C-600: (A) XANES, (B) FT-EXAFS spectra of Co-C-600.

the following order: Co-C-700 >Co-C-600 >Co-C-500. This demonstrated that the contribution of direct electron transfer to the SMX degradation for Co-C-700 was the highest, which could be due to the increase of graphitic carbon with the increase of pyrolysis temperature [61]. The degradation of organic pollutants driven by direct electron transfer was hardly affected by the water components [62], which explained the slight inhibition of ethanol, tertiary butanol and benzoquinone.

In summary, radicals and high-valent cobalt-oxo as well as the surface-mediated electron transfer contributed to the SMX degradation. But the contribution of each way to SMX degradation varied with the pyrolysis temperature. It is noted that both cobalt existed as CoO in both Co-C-500 and Co-C-700, but the catalytic activity of Co-C-500 and Co-C-700 was significantly different. The possible reasons might be due to the different carbon framework, cobalt content and cobalt size. It is thus concluded that pyrolysis temperature of Co-C-X could modulate activation mechanism of PMS.

3.4. Catalytic mechanism of Co-C-X

Co-C-500 was consisted of g-C_3N_4 and CoO. The activation mechanism of PMS by metal oxide supported on the g-C_3N_4 has been widely investigated. The metal and its oxide supported on the g-C_3N_4 could activate PMS to produce radicals [63,64], while the Co-N bond could adsorb PMS to produce high-valent cobalt-oxo via oxygen transfer [65]. The modified carbon framework could activate PMS to produce singlet oxygen [63]. In addition, the modified g-C_3N_4 could also sever as electron mediator to promote the SMX degradation as evidenced by the significant current (Fig. S7). Based on the identified reactive species in the system of Co-C-500/PMS, PMS activation mechanism by Co-C-500 was due to the synergistic effect of CoO, Co-N and modified g-C_3N_4. Specifically, the modified g-C_3N_4 was mainly responsible for the non-radicals pathway, while the cobalt active sites were mainly responsible for the pathways of radicals and high-valent cobalt-oxo.

Co-C-600 was consisted of single atom Co and graphitic carbon. For SAC-Co, Co-Nx was widely considered as the main active sites for PMS activation. But the produced reactive species varied with the coordination structure of Co single atom. XAFs analysis was thus used to determine the coordination structure of Co single atom. XANES showed that
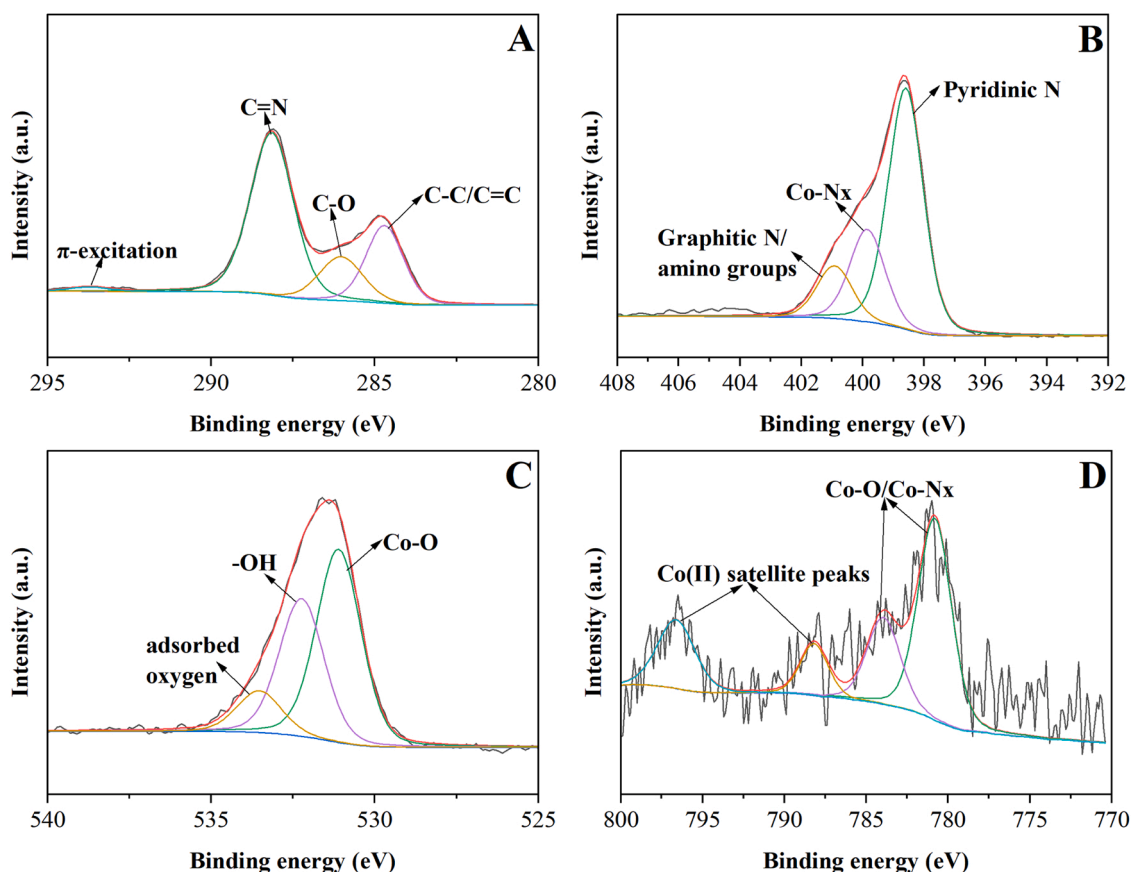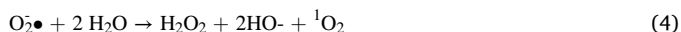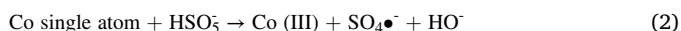
Fig. 7. XPS analysis of Co-C-600 after reaction (A) C1s (B) N1s (C) O1s (D) Co2p.

the rising edge for Co was located between Co and CoO, indicating that Co valence state was in between 0 and + 2 (Fig. 6A). The coordination structure of Co-C-600 was further determined by the extended X-ray absorption fine structure (EXAFS) spectra (Fig. 6B). A significant peak appeared at 1.44 Å, which corresponded to Co−N shell [66].

The valence of Co indicated that Co could provide electron for PMS activation to produce radicals (Eqs. (1) and (2)). Subsequently, the produced Co(III) could further adsorb PMS to produce high-valent cobalt-oxo via Co-N bond like Fe(III)-N bond [65].

$$Co\ single\ atom + HSO_5^- \rightarrow Co\ (III) + SO_4\bullet^- + HO^- \quad (2)$$

$$Co\ single\ atom + HSO_5^- \rightarrow Co(III) + HO\bullet + SO_4^{2-} \quad (3)$$

$$O_2^-\bullet + 2\ H_2O \rightarrow H_2O_2 + 2HO- + {}^1O_2 \quad (4)$$

The formation of singlet oxygen could proceed via the following pathway. Firstly, singlet oxygen could derive from the PMS self-decomposition. However, the solution pH was 3.4 in which PMS is stable [9]. In this case the PMS self-decomposition could be neglected. Secondly, it could be due to the PMS activation by oxygen-containing functional groups in the carbon framework [49,67]. Thirdly, it could be attributed to the recombination of superoxide radicals (Eq. (3)). However, the above results (3.3 section) has denied the formation of superoxide radicals during the process of PMS activation. It is thus concluded that carbon framework played major role in the formation of singlet oxygen.

To further verify the above deduction, XPS spectrums of Co-C-X after reaction were investigated (Fig. 7). The components of each element had no change before and after reaction. The proportion of C1s components kept almost unchanged before and after reaction. But the binding energy of C-O functional groups decreased by 0.2 eV. Similarly, the components' proportion of N1s and Co2p had no changed before and after

reaction. But the binding energy of Co-Nx and Co-O increased, suggesting that Co-Nx/Co-O provided electron, which is consistent with the results of XANES. For O1s, the proportion of Co-O functional groups increased after reaction, while the proportion of –OH and adsorbed oxygen decreased. The binding energy of Co-O, -OH and adsorbed oxygen increased. The increase of binding energy of components indicated that it acted as electron donor, while the decrease of binding energy of components suggesting that it acted as electron acceptor [49,68]. Thus, the Co-Nx/Co-O, pyridinic N, -OH and adsorbed oxygen acted as electron donor for PMS to produce radicals, while C-O acted as electron acceptor for PMS to produce singlet oxygen.

It is noted that atrazine degradation was faster than that of nitrobenzene at 5 min (Fig. S6), indicating that the yield of sulfate radicals was higher than that of hydroxyl radicals within 5 min. Afterwards, the degradation rates of atrazine and nitrobenzene were almost the same until 30 min. Thereafter, the degradation of nitrobenzene became much slower than that of atrazine. Based on the above phenomenon, it is thus concluded that hydroxyl radicals was derived from the sulfate radicals, and the contribution of hydroxyl radicals mainly occurred within 30 min. Sulfate radicals can be converted into hydroxyl radicals through the following pathways (Eq. (4) and Eq. (5)).

$$SO_4\bullet^- + H_2O \rightarrow HO\bullet + SO_4^{2-} + H^+ \quad (4)$$

$$SO_4\bullet^- + HO^- \rightarrow HO\bullet + SO_4^{2-} \quad (5)$$

The above deduction was proved by the high resolution spectrums of O1s (Fig. 7C). The proportion of -OH and adsorbed oxygen decreased after reaction for Co-C-600, indicating the transformation of -OH and adsorbed oxygen into HO•.

In addition, dissolved cobalt ions could activate PMS to produce sulfate radicals. To verify the contribution of dissolved cobalt in solution to the SMX degradation, the SMX degradation was investigated in the
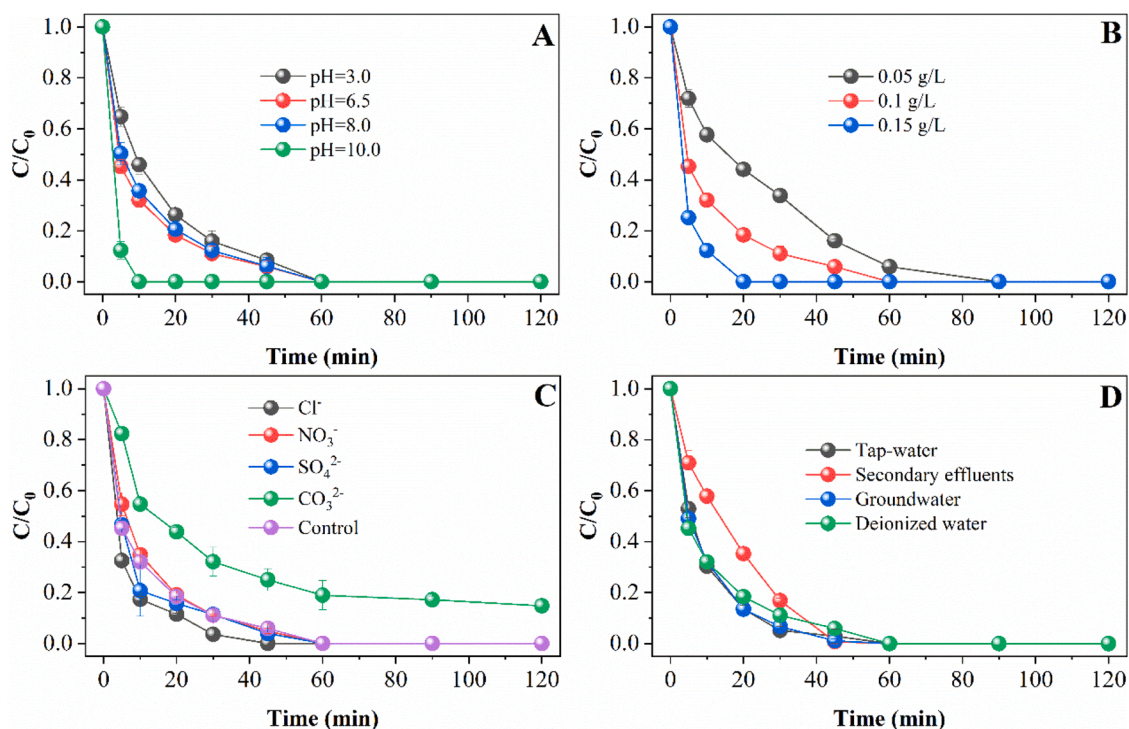
Fig. 8. Influential factors on the SMX degradation by Co-C-600-activated PMS (A) pH (B) Co-C-600 dosage (C) inorganic ions (D) water components. General conditions: [SMX]= 0.04 mM, [PMS]= 0.4 mM, [Inorganic ion]= 10 mM, Co-C-600 dosage of 0.1 g/L, pH 3.2, 25 °C.

system of Co(II)/PMS with different concentration of Co(II). The degradation rate of SMX increased with the increase of Co(II) concentration (Fig. S8). When the concentration of Co(II) was 0.5 mg/L, its degradation rate of SMX was 0.024 min^{-1}, which was much lower than that in the systems of Co-C-500 and Co-C-600/PMS. Moreover, the concentration of dissolved cobalt was less than 0.5 mg/L for Co-C-500 and Co-C-600. Based on the above reasons, it is thus concluded that dissolved cobalt made minor contribution to SMX degradation. Similarly, for Co-C-700, the concentration of dissolved cobalt was lower than 5 mg/L, but the degradation rate of SMX was much higher than that in the presence of 5 mg/L Co(II). Thus, the dissolved cobalt made minor contribution to SMX degradation.

Similar to Co-C-500, Co-C-700 also consisted CoO. But the size of CoO on the Co-C-700 was smaller than that on the Co-C-500 (Fig. 3C). In addition, compared with Co-C-500, the carbon framework of Co-C-700 was not g-C$_3$N$_4$, but graphitic carbon. Graphitic carbon had better electron transfer capacity than g-C$_3$N$_4$ as evidenced by the higher current (Fig. S7). Thus, for Co-C-700, the contribution of direct electron transfer contributed more to the SMX degradation than for Co-C-500. In addition, Co-C-700 produced higher steady concentration of hydroxyl radicals and sulfate radicals than Co-C-500, which could be due to the concentration of high dissolved cobalt and small size cobalt as well as high content of cobalt. In summary, for Co-C-700, the cobalt sites served as the main active sites for the pathways of radicals and high-valent Co, while graphitic carbon framework was mainly responsible for non-radicals pathway.

Considering that the environmental quality standards for Co in surface water (1 mg/L, GB 3838–2002, China) and the catalytic activity, Co-C-600 was thus selected to conduct the experiments of influential factors.

3.5. Catalytic performance under different conditions

pH affected the catalytic performance of Co-C-600 (Fig. 8A). When the solution pH increased from 3 to 6.5. The SMX degradation rate was increased. When solution pH was further increased to 8.0, no significant

variation was found for the SMX degradation. When the solution pH was increased to 10.0, the SMX degradation rate was accelerated. SMX was completely removed within 10 min. When the solution pH was 3.0, the concentration of hydrogen ion was high, which may inhibit the yield of hydroxyl radicals resulting in the decrease of SMX. In addition, when solution pH was higher 5.7, SMX existed as anions that has higher reaction rate with radicals than neutral SMX [69,70]. When the solution pH was increased to 10, the concentration of hydroxyl ions increased, which may promote the formation of hydroxyl radicals by Eq. (5). In addition, high solution pH may depress the formation of high-valent cobalt-oxo [24]. In this case cobalt active sites tended to produce radicals that accelerated the degradation of SMX.

The increase of Co-C-600 dosage accelerated the SMX degradation (Fig. 8B), which was due to the increased number of active sites of PMS. When the dosage of Co-C-600 increased to 0.15 g/L, the SMX mineralization could achieve 58.7%.

Common anions including chloride, nitrate, carbonate and sulfate ions showed differentiate effect on SMX degradation (Fig. 8C). Chloride ions promoted the SMX degradation, which could be due to the homogeneous direct reaction between chloride and PMS resulting in the formation of hypochlorite acid that could remove SMX [71]. Nitrate and sulfate ions showed no significant effect on the SMX degradation, while carbonate ions showed significant inhibition that might be due to the variation of solution pH caused by the carbonate ions [72]. Considering that high pH had no inhibition on the SMX degradation (Fig. 8A), the inhibition of carbonate ions may be due to the competition of carbonate ions for the active sites. Furthermore, the carbonate ions may affect the direct electron transfer [73]. In addition, the carbonate radicals could be formed due to the reaction between carbonate and sulfate radicals/hydroxyl radicals. Carbonate radicals had lower oxidizing capacity compared with sulfate radicals/hydroxyl radicals resulting in the decrease of SMX degradation [74]. All the above reasons resulted in the significant inhibition of carbonate ions on the SMX degradation.

The performance of Co-C-600 in different water components was investigated (Fig. 8D). The water components of tap-water, secondary effluents and groundwater were listed in Table S3. SMX degradation had
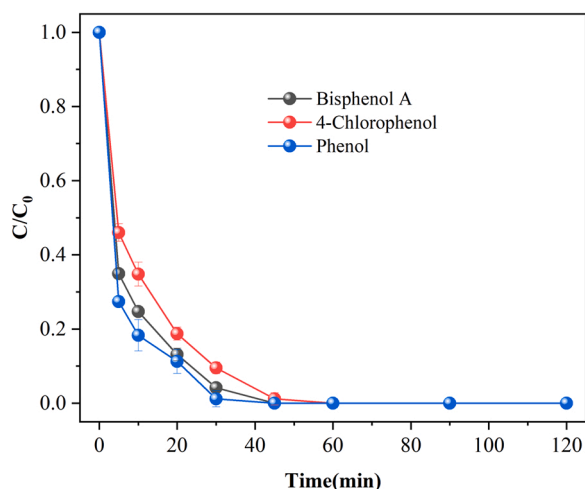
Fig. 9. Oxidation capacity of Co-C-600/PMS system. [Bisphenol A]= [4-chlorophenol]= [phenol]= 10 mg/L, [PMS]= 0.4 mM, Co-C-600 dosage of 0.1 g/L, pH 3.2, 25 °C.

no obvious variation in tap-water and groundwater compared to that in deionized water. In contrast, SMX degradation was significant depressed in secondary effluents, which could be due to the presence of organic pollutants that could compete with radicals. But SMX was still completely removed at the end.

In addition to the above mentioned emerging organic pollutants (SMX, nitrobenzene and atrazine), Co-C-600/PMS could also remove bisphenol A, 4-chlorophenol and phenol (Fig. 9), further demonstrating that Co-C-600/PMS had strong oxidizing capacity that can remove a wide range of organic pollutants. Furthermore, Co-C-600 could also activate peroxydisulfate as evidenced by the significant SMX degradation. Moreover, the SMX degradation was accelerated when the concentration of peroxydisulfate was increased from 0.8 to 1.6 mM (Fig. S9). Co-C-600 showed different activation capacity to PMS and peroxydisulfate, which could be due to the different structure of O-O bond in PMS and peroxydisulfate.

3.6. Catalytic stability

Catalytic stability of Co-C-600 was investigated by cycling experiments. As shown in Fig. S10, SMX was completely removed in the consecutive five cycling experiments. The concentration of dissolved cobalt was 0.14, 0.11, 0.21, 0.16 and 0.13 mg/L, respectively for the consecutive five cycling experiments, further demonstrating that Co-C-600 had superior catalytic stability.

4. Conclusions

This study provided a facile way to synthesize the Co single atom catalyst that could effectively activate PMS for the degradation of organic pollutants. Co-C-X could activate PMS to produce radicals, high-valent cobalt-oxo and singlet oxygen that contributed to high catalytic activity. Pyrolysis temperature could adjust the coordination structure of cobalt atoms that further regulated the contribution of different reactive species to the degradation of targeted organic pollutants. Co-C-600 showed the optimal catalytic activity and stability. In addition, Co-C-600 showed wide pH application range. In general, this study provided an effective PMS activator for the removal of emerging organic pollutants and a way to modulate the concentration of reactive species derived from PMS activation by modulating pyrolysis temperature.

CRediT authorship contribution statement

Shizong Wang: Investigation, Formal analysis, Writing – original draft. **Jianlong Wang:** Conceptualization, Writing – review & editing.

Declaration of Competing Interest

The authors declare that they have no known competing financial interests or personal relationships that could have appeared to influence the work reported in this paper.

Data Availability

Data will be made available on request.

Acknowledgements

Appendix A. Supporting information

Supplementary data associated with this article can be found in the online version at doi:10.1016/j.apcatb.2022.122051.

References

[1] M.B. Gawande, P. Fornasiero, R. Zbořil, Carbon-based single-atom catalysts for advanced applications, ACS Catal. 10 (2020) 2231–2259.

[2] Y. Shang, X. Xu, B. Gao, S. Wang, X. Duan, Single-atom catalysis in advanced oxidation processes for environmental remediation, Chem. Soc. Rev. 50 (2021) 5281–5322.

[3] S.K. Kaiser, Z. Chen, D. Faust Akl, S. Mitchell, J. Pérez-Ramírez, Single-atom catalysts across the periodic table, Chem. Rev. 120 (2020) 11703–11809.

[4] K. Huang, L. Zhang, T. Xu, H. Wei, R. Zhang, X. Zhang, B. Ge, M. Lei, J.Y. Ma, L. M. Liu, H. Wu, −60 °C solution synthesis of atomically dispersed cobalt electrocatalyst with superior performance, Nat. Commun. 10 (2019) 606.

[5] A. Wang, J. Li, T. Zhang, Heterogeneous single-atom catalysis, Nat. Rev. Chem. 2 (2018) 65–81.

[6] F. Li, G.F. Han, H.J. Noh, S.J. Kim, Y. Lu, H. Young Jeong, Z. Fu, J.B. Baek, Boosting oxygen reduction catalysis with abundant copper single atom active sites, Energy Environ. Sci. 11 (2018) 2263–2269.

[7] Y. Xiong, H. Li, C. Liu, L. Zheng, C. Liu, J. Wang, S. Liu, Y. Han, L. Gu, J. Qian, D. Wang, Single-atom Fe catalysts for Fenton-like reactions: roles of different N species, Adv. Mater. 34 (2022) 2110653.

[8] F. Chen, X.-L. Wu, C. Shi, H. Lin, J. Chen, Y. Shi, S. Wang, X. Duan, Molecular engineering toward pyrrolic N-rich M-N$_4$ (M = Cr, Mn, Fe, Co, Cu) single-atom sites for enhanced heterogeneous fenton-like reaction, Adv. Funct. Mater. 31 (2021) 2007877.

[9] J.L. Wang, S.Z. Wang, Activation of persulfate (PS) and peroxymonosulfate (PMS) and application for the degradation of emerging contaminants, Chem. Eng. J. 334 (2018) 1502–1517.

[10] L. Peng, X. Duan, Y. Shang, B. Gao, X. Xu, Engineered carbon supported single iron atom sites and iron clusters from Fe-rich *Enteromorpha* for Fenton-like reactions via nonradical pathways, Appl. Catal. B: Environ. 287 (2021), 119963.

[11] W. Yang, M. Zhao, X. Ding, K. Ma, C. Wu, I.D. Gates, Z. Gao, The effect of coordination environment on the kinetic and thermodynamic stability of single-atom iron catalysts, Phys. Chem. Chem. Phys. 22 (2020) 3983–3989.

[12] X. Mi, P. Wang, S. Xu, S. Xu, L. Su, H. Zhong, H. Wang, Y. Li, S. Zhan, Almost 100% peroxymonosulfate conversion to singlet oxygen on single-atom CoN$_{2+2}$ Sites, Angew. Chem. Int. Ed. 60 (2021) 4588–4593.

[13] G. Wang, X. Nie, X. Ji, X. Quan, S. Chen, H. Wang, H. Yu, X. Guo, Enhanced heterogeneous activation of peroxymonosulfate by Co and N codoped porous carbon for degradation of organic pollutants: the synergism between Co and N, Environ. Sci.: Nano 6 (2019) 399–410.

[14] X. Li, X. Huang, S. Xi, S. Miao, J. Ding, W. Cai, S. Liu, X. Yang, H. Yang, J. Gao, J. Wang, Y. Huang, T. Zhang, B. Liu, Single cobalt atoms anchored on porous N-doped graphene with dual reaction sites for efficient Fenton-like catalysis, J. Am. Chem. Soc. 140 (2018) 12469–12475.

[15] Y. Gao, C. Yang, M. Zhou, C. He, S. Cao, Y. Long, S. Li, Y. Lin, P. Zhu, C. Cheng, Transition metal and metal–Nx codoped mof-derived Fenton-like catalysts: a comparative study on single atoms and nanoparticles, Small 16 (2020) 2005060.

[16] X. Li, H. Rong, J. Zhang, D. Wang, Y. Li, Modulating the local coordination environment of single-atom catalysts for enhanced catalytic performance, Nano, Research 13 (2020) 1842–1855.

[17] J. Zhang, Y. Zhao, C. Chen, Y.-C. Huang, C.-L. Dong, C.-J. Chen, R.-S. Liu, C. Wang, K. Yan, Y. Li, G. Wang, Tuning the coordination environment in single-atom catalysts to achieve highly efficient oxygen reduction reactions, J. Am. Chem. Soc. 141 (2019) 20118–20126.

[18] Y. Zhang, J. Yang, R. Ge, J. Zhang, J.M. Cairney, Y. Li, M. Zhu, S. Li, W. Li, The effect of coordination environment on the activity and selectivity of single-atom catalysts, Coord. Chem. Rev. 461 (2022), 214493.

[19] Y. Qi, J. Li, Y. Zhang, Q. Cao, Y. Si, Z. Wu, M. Akram, X. Xu, Novel lignin-based single atom catalysts as peroxymonosulfate activator for pollutants degradation: Role of single cobalt and electron transfer pathway, Appl. Catal. B: Environ. 286 (2021), 119910.

[20] H. Song, R. Du, Y. Wang, D. Zu, R. Zhou, Y. Cai, F. Wang, Z. Li, Y. Shen, C. Li, Anchoring single atom cobalt on two-dimensional MXene for activation of peroxymonosulfate, Appl. Catal. B: Environ. 286 (2021), 119898.

[21] S.Z. Wang, J.L. Wang, Magnetic 2D/2D oxygen doped g-C$_3$N$_4$/biochar composite to activate peroxymonosulfate for degradation of emerging organic pollutants, J. Hazard. Mater. 423 (2022), 127207.

[22] G.V. Buxton, C.L. Greenstock, W.P. Helman, A.B. Ross, Critical review of rate constants for reactions of hydrated electrons, hydrogen atoms and hydroxyl radicals (·OH/·O$^-$ in aqueous solution, J. Phys. Chem. Ref. Data 17 (1988) 513–886.

[23] D.S. Shtarev, A.V. Shtareva, A.I. Blokh, P.S. Goncharova, K.S. Makarevich, On the question of the optimal concentration of benzoquinone when it is used as a radical scavenger, Appl. Phys. A 123 (2017) 602.

[24] Y. Zong, X. Guan, J. Xu, Y. Feng, Y. Mao, L. Xu, H. Chu, D. Wu, Unraveling the overlooked involvement of high-valent cobalt-oxo species generated from the cobalt(II)-activated peroxymonosulfate process, Environ. Sci. Technol. 54 (2020) 16231–16239.

[25] N. Ranjbar Sahraie, J.P. Paraknowitsch, C. Göbel, A. Thomas, P. Strasser, Noble-metal-free electrocatalysts with enhanced orr performance by task-specific functionalization of carbon using ionic liquid precursor systems, J. Am. Chem. Soc. 136 (2014) 14486–14497.

[26] O.Y. Bisen, R. Nandan, A.K. Yadav, B. Pavithra, K. Kar, Nanda, In situ self-organization of uniformly dispersed Co–N–C centers at moderate temperature without a sacrificial subsidiary metal, Green. Chem. 23 (2021) 3115–3126.

[27] J.L. Wang, S.Z. Wang, A critical review on graphitic carbon nitride (g-C$_3$N$_4$)-based materials: preparation, modification and environmental application, Coord. Chem. Rev. 453 (2022), 214338.

[28] X. Wu, D. Gao, P. Wang, H. Yu, J. Yu, NH$_4$Cl-induced low-temperature formation of nitrogen-rich g-C$_3$N$_4$ nanosheets with improved photocatalytic hydrogen evolution, Carbon 153 (2019) 757–766.

[29] Y. Zhou, L. Zhang, W. Huang, Q. Kong, X. Fan, M. Wang, J. Shi, N-doped graphitic carbon-incorporated g-C$_3$N$_4$ for remarkably enhanced photocatalytic H$_2$ evolution under visible light, Carbon 99 (2016) 111–117.

[30] S. Yang, Y. Gong, J. Zhang, L. Zhan, L. Ma, Z. Fang, R. Vajtai, X. Wang, P. M. Ajayan, Exfoliated graphitic carbon nitride nanosheets as efficient catalysts for hydrogen evolution under visible light, Adv. Mater. 25 (2013) 2452–2456.

[31] C. Chang, Y. Fu, M. Hu, C. Wang, G. Shan, L. Zhu, Photodegradation of Bisphenol A by highly stable palladium-doped mesoporous graphite carbon nitride (Pd/mpg-C$_3$N$_4$) under simulated solar light irradiation, Appl. Catal. B: Environ. 142–143 (2013) 553–560.

[32] R. Wang, H. Wu, R. Chen, Y. Chi, Strong Electrochemiluminescence emission from oxidized multiwalled carbon nanotubes, Small 15 (2019) 1901550.

[33] M.P. Suryawanshi, U.V. Ghorpade, S.W. Shin, U.P. Suryawanshi, H.J. Shim, S. H. Kang, J.H. Kim, Facile, Room temperature, electroless deposited (Fe$_{1-x}$Mn$_x$) OOH nanosheets as advanced catalysts: the role of Mn incorporation, Small 14 (2018) 1801226.

[34] Z. Zhou, Q. Zhang, J. Sun, B. He, J. Guo, Q. Li, C. Li, L. Xie, Y. Yao, Metal–organic framework derived spindle-like carbon incorporated α-Fe$_2$O$_3$ grown on carbon nanotube fiber as anodes for high-performance wearable asymmetric supercapacitors, ACS Nano 12 (2018) 9333–9341.

[35] K. Artyushkova, B. Kiefer, B. Halevi, A. Knop-Gericke, R. Schlogl, P. Atanassov, Density functional theory calculations of XPS binding energy shift for nitrogen-containing graphene-like structures, Chem. Commun. 49 (2013) 2539–2541.

[36] W. Zhang, C.-H. Xu, H. Zheng, R. Li, K. Zhou, Oxygen-rich cobalt–nitrogen–carbon porous nanosheets for bifunctional oxygen electrocatalysis, Adv. Funct. Mater. 33 (2022) 2200763.

[37] D. He, X. Song, W. Li, C. Tang, J. Liu, Z. Ke, C. Jiang, X. Xiao, Active electron density modulation of Co$_3$O$_4$-based catalysts enhances their oxygen evolution performance, Angew. Chem. Int. Ed. 59 (2020) 6929–6935.

[38] S. Wang, Q. He, C. Wang, H. Jiang, C. Wu, S. Chen, G. Zhang, L. Song, Active sites engineering toward superior carbon-based oxygen reduction catalysts via confinement pyrolysis, Small 14 (2018) 1800128.

[39] W. Niu, Z. Xiao, S. Wang, S. Zhai, L. Qin, Z. Zhao, Q. An, Z. Li, Porous NiCoP@P–C hybrid as efficient positive electrodes for high-performance supercapacitors, J. Alloy. Compd. 835 (2020), 155157.

[40] Y. Qi, L. Zhang, L. Sun, G. Chen, Q. Luo, H. Xin, J. Peng, Y. Li, F. Ma, Sulfur doping enhanced desorption of intermediates on NiCoP for efficient alkaline hydrogen evolution, Nanoscale 12 (2020) 1985–1993.

[41] E. Dervishi, Z. Ji, H. Htoon, M. Sykora, S.K. Doorn, Raman spectroscopy of bottom-up synthesized graphene quantum dots: size and structure dependence, Nanoscale 11 (2019) 16571–16581.

[42] D. Sun, B. Luo, H. Wang, Y. Tang, X. Ji, L. Wang, Engineering the trap effect of residual oxygen atoms and defects in hard carbon anode towards high initial Coulombic efficiency, Nano Energy 64 (2019), 103937.

[43] P. Su, W. Huang, J. Zhang, U. Guharoy, Q. Du, Q. Sun, Q. Jiang, Y. Cheng, J. Yang, X. Zhang, Y. Liu, S.P. Jiang, J. Liu, Fe atoms anchored on defective nitrogen doped hollow carbon spheres as efficient electrocatalysts for oxygen reduction reaction, Nano, Research 14 (2021) 1069–1077.

[44] J. Wang, Y. Xu, B. Ding, Z. Chang, X. Zhang, Y. Yamauchi, K.C.-W. Wu, Confined self-assembly in two-dimensional interlayer space: monolayered mesoporous carbon nanosheets with in-plane orderly arranged mesopores and a highly graphitized framework, Angew. Chem. Int. Ed. 57 (2018) 2894–2898.

[45] J. Tang, J. Liu, C. Li, Y. Li, M.O. Tade, S. Dai, Y. Yamauchi, Synthesis of nitrogen-doped mesoporous carbon spheres with extra-large pores through assembly of diblock copolymer micelles, Angew. Chem. Int. Ed. 54 (2015) 588–593.

[46] Y. Pang, S. Chen, C. Xiao, S. Ma, S. Ding, MOF derived CoO-NCNTs two-dimensional networks for durable lithium and sodium storage, J. Mater. Chem. A 7 (2019) 4126–4133.

[47] S.Z. Wang, L.J. Xu, J.L. Wang, Iron-based dual active site-mediated peroxymonosulfate activation for the degradation of emerging organic pollutants, Environ. Sci. Technol. 55 (2021) 15412–15422.

[48] P. Gao, X. Tian, W. Fu, Y. Wang, Y. Nie, C. Yang, Y. Deng, Copper in LaMnO$_3$ to promote peroxymonosulfate activation by regulating the reactive oxygen species in sulfamethoxazole degradation, J. Hazard. Mater. 411 (2021), 125163.

[49] S.Z. Wang, Y. Liu, J.L. Wang, Peroxymonosulfate Activation by Fe–Co–O-codoped graphite carbon nitride for degradation of sulfamethoxazole, Environ. Sci. Technol. 54 (2020) 10361–10369.

[50] M. Xu, H. Zhou, Z. Wu, N. Li, Z. Xiong, G. Yao, B. Lai, Efficient degradation of sulfamethoxazole by NiCo$_2$O$_4$ modified expanded graphite activated peroxymonosulfate: characterization, mechanism and degradation intermediates, J. Hazard. Mater. 399 (2020), 123103.

[51] F. Chen, X.-L. Wu, L. Yang, C. Chen, H. Lin, J. Chen, Efficient degradation and mineralization of antibiotics via heterogeneous activation of peroxymonosulfate by using graphene supported single-atom Cu catalyst, Chem. Eng. J. 394 (2020), 124904.

[52] J. Wang, B. Li, Y. Li, X. Fan, F. Zhang, G. Zhang, W. Peng, Facile synthesis of atomic Fe-N-C materials and dual roles investigation of Fe-N$_4$ sites in Fenton-like reactions, Advanced, Science 8 (2021) 2101824.

[53] K. Im, J.-H. Jang, J. Heo, D. Kim, K.-S. Lee, H.-K. Lim, J. Kim, S.J. Yoo, Design of Co-NC as efficient electrocatalyst: The unique structure and active site for remarkable durability of proton exchange membrane fuel cells, Appl. Catal. B: Environ. 308 (2022), 121220.

[54] W. Liu, L. Zhang, X. Liu, X. Liu, X. Yang, S. Miao, W. Wang, A. Wang, T. Zhang, Discriminating catalytically active fenx species of atomically dispersed Fe–N–C catalyst for selective oxidation of the C–H bond, J. Am. Chem. Soc. 139 (2017) 10790–10798.

[55] A.L. Boreen, W.A. Arnold, K. McNeill, Photochemical fate of sulfa drugs in the aquatic environment: sulfa drugs containing five-membered heterocyclic groups, Environ. Sci. Technol. 38 (2004) 3933–3940.

[56] N.E. Rojas, Hosse, Kinetics of trace organics degradation by singlet oxygen indirect photolysis, The University of Arizona, Ann. Arbor (2020) 66.

[57] E.-T. Yun, G.-H. Moon, H. Lee, T.H. Jeon, C. Lee, W. Choi, J. Lee, Oxidation of organic pollutants by peroxymonosulfate activated with low-temperature-modified nanodiamonds: Understanding the reaction kinetics and mechanism, Appl. Catal. B: Environ. 237 (2018) 432–441.

[58] A. Di Corcia, C. Crescenzi, E. Guerriero, R. Samperi, Ultratrace determination of atrazine and its six major degradation products in water by solid-phase extraction and liquid chromatography–electrospray/mass spectrometry, Environ. Sci. Technol. 31 (1997) 1658–1663.

[59] Y. Yang, J. Jiang, X. Lu, J. Ma, Y. Liu, Production of sulfate radical and hydroxyl radical by reaction of ozone with peroxymonosulfate: a novel advanced oxidation process, Environ. Sci. Technol. 49 (2015) 7330–7339.

[60] E.-T. Yun, J.H. Lee, J. Kim, H.-D. Park, J. Lee, Identifying the nonradical mechanism in the peroxymonosulfate activation process: singlet oxygenation versus mediated electron transfer, Environ. Sci. Technol. 52 (2018) 7032–7042.

[61] S.Z. Wang, J.L. Wang, Nitrogen doping sludge-derived biochar to activate peroxymonosulfate for degradation of sulfamethoxazole: Modulation of degradation mechanism by calcination temperature, J. Hazard. Mater. 418 (2021), 126309.

[62] Y. Ding, X. Wang, L. Fu, X. Peng, C. Pan, Q. Mao, C. Wang, J. Yan, Nonradicals induced degradation of organic pollutants by peroxydisulfate (PDS) and peroxymonosulfate (PMS): Recent advances and perspective, Sci. Total Environ. 765 (2021), 142794.

[63] S.Z. Wang, Y. Liu, J.L. Wang, Iron and sulfur co-doped graphite carbon nitride (FeO$_y$/S-g-C$_3$N$_4$) for activating peroxymonosulfate to enhance sulfamethoxazole degradation, Chem. Eng. J. 382 (2020), 122836.

[64] Z. Huang, M. Shen, J. Liu, J. Ye, T. Asefa, Facile synthesis of an effective g-C$_3$N$_4$-based catalyst for advanced oxidation processes and degradation of organic compounds, J. Mater. Chem. A 9 (2021) 14841–14850.

[65] H. Li, C. Shan, B. Pan, Fe(III)-Doped g-C$_3$N$_4$ mediated peroxymonosulfate activation for selective degradation of phenolic compounds via high-valent iron-oxo species, Environ. Sci. Technol. 52 (2018) 2197–2205.

[66] K. Huang, C. Wei, J. Liu, Z. Gong, J. Liu, M. Yan, G. He, H. Gong, Y. Hu, Y. He, S. Zhao, G. Ye, H. Fei, Engineering the morphology and microenvironment of a graphene-supported Co-N-C single-atom electrocatalyst for enhanced hydrogen evolution, Small 18 (2022) 2201139.

[67] P. Liang, C. Zhang, X. Duan, H. Sun, S. Liu, M.O. Tade, S. Wang, N-doped graphene from metal–organic frameworks for catalytic oxidation of p-hydroxylbenzoic acid: N-functionality and mechanism, ACS Sustain. Chem. Eng. 5 (2017) 2693–2701.

[68] K.M. Fair, X.Y. Cui, L. Li, C.C. Shieh, R.K. Zheng, Z.W. Liu, B. Delley, M.J. Ford, S. P. Ringer, C. Stampfl, Hydrogen adsorption capacity of adatoms on double carbon vacancies of graphene: a trend study from first principles, Phys. Rev. B 87 (2013), 014102.

[69] J. Zhang, J. Li, H. Su, Y. Zhao, X. Zeng, M. Hu, W. Xiao, X. Mao, H-bonding effect of oxyanions enhanced photocatalytic degradation of sulfonamides by g-C$_3$N$_4$ in aqueous solution, J. Hazard. Mater. 366 (2019) 259–267.

[70] Y. Yang, X. Lu, J. Jiang, J. Ma, G. Liu, Y. Cao, W. Liu, J. Li, S. Pang, X. Kong, C. Luo, Degradation of sulfamethoxazole by UV, UV/H$_2$O$_2$ and UV/persulfate (PDS): Formation of oxidation products and effect of bicarbonate, Water Res. 118 (2017) 196–207.

[71] J.L. Wang, S.Z. Wang, Effect of inorganic anions on the performance of advanced oxidation processes for degradation of organic contaminants, Chem. Eng. J. 411 (2021), 128392.

[72] S.Z. Wang, H.Y. Liu, J.L. Wang, Nitrogen, sulfur and oxygen co-doped carbon-armored Co/Co$_9$S$_8$ rods (Co/Co$_9$S$_8$@N-S-O-C) as efficient activator of peroxymonosulfate for sulfamethoxazole degradation, J. Hazard. Mater. 387 (2020) 121669.

[73] E. Ferapontova, L. Gorton, Effect of pH on direct electron transfer in the system gold electrode–recombinant horseradish peroxidase, Bioelectrochemistry 55 (2002) 83–87.

[74] J.L. Wang, S.Z. Wang, Reactive species in advanced oxidation processes: formation, identification and reaction mechanism, Chem. Eng. J. 401 (2020), 126158.